Solar Energy 171 (2018) 122–129

Contents lists available at ScienceDirect

Solar Energy

journal homepage: www.elsevier.com/locate/solener

CuS/WS_2 and CuS/MoS_2 heterostructures for high performance counter electrodes in dye-sensitized solar cells

Sajjad Hussain[a,b,1], Supriya A. Patil[c,d,1], Anam Ali Memon[g], Dhanasekaran Vikraman[f], Bilal Abbas Naqvi[a,b], Sung Hoon Jeong[e], Hyun-Seok Kim[f], Hak-Sung Kim[c,d,*], Jongwan Jung[a,b,*]

[a] Graphene Research Institute, Sejong University, Seoul 143-747, Republic of Korea
[b] Institute of Nano and Advanced Materials Engineering, Sejong University, Seoul 143-747, Republic of Korea
[c] Department of Mechanical Engineering, Hanyang University, Haengdang-dong, Seongdong-gu, 133-791 Seoul, Republic of Korea
[d] Institute of Nano Science and Technology, Hanyang University, Seoul 133-79, Republic of Korea
[e] Department of Organic and Nano Engineering, Hanyang University, Seoul 133-791, Republic of Korea
[f] Division of Electronics and Electrical Engineering, Dongguk University-Seoul, Seoul 04620, Republic of Korea
[g] Department of Textile Engineering, Mehran University of Engineering and Technology , Jamshoro Sindh, Pakistan

ARTICLE INFO

Keywords:
TMD
Heterostructure
Sputtering
CEs
DSSC

ABSTRACT

In this work, we demonstrated CuS/WS_2 and CuS/MoS_2 heterostructures via a sputtering-CVD process for dye-sensitized solar cells (DSSCs) as a counter electrode (CE) to replace the currently preferred expensive platinum (Pt). The cyclic voltammetry, electrochemical impedance spectroscopy, and Tafel curve studies revealed that the unique CuS/WS_2 and CuS/MoS_2 heterostructures were beneficial in achieving high electrocatalytic activity, low charge-transfer resistance at the CE/electrolyte interface, and fast reaction kinetics for the reduction of triiodide to iodide at the CE. The constructed DSSCs using these CuS/WS_2 and CuS/MoS_2 CEs exhibited high-power conversion efficiencies (PCEs) of 8.21% and 7.12%, respectively, which are comparable to conventional Pt CE (8.74%) and pristine WS_2, MoS_2, and CuS CEs (6.0%, 6.3% and 6.4%). This novel sulfur based heterostructure opens up opportunities for a variety of optoelectronic and photoelectrochemical applications.

1. Introduction

Dye-sensitized solar cells (DSSCs) have made remarkable progress as an alternative to conventional silicon based solar cells, owing to their low cost, low energy consumption, environmental friendliness, easy fabrication process, reproducibility, and high-power conversion efficiency (Grätzel, 2001; O'regan and Grätzel, 1991; Yella et al., 2011). Typically, a DSSC has a sandwich structure with a photoanode (a thin layer of titanium dioxide (TiO_2) on the back of the conductive plate sensitized by a dye), a thin iodide electrolyte layer containing the triiodide (I_3^-)/iodide (I^-) redox couple, and a counter electrode (CE). So far, platinum (Pt) has been used as a CE to catalyze the reduction of I_3^- to I^- in large-scale manufacturing of DSSCs. However, platinum is a scarce and high cost noble metal with a low abundance ratio and requires high temperature annealing (Xin et al., 2011), which limits the commercialization of DSSCs. Recently, two dimensional (2D)-layered materials have gained tremendous scientific and industrial attention for DSSCs as electrocatalysts, such as metal sulfides (Bi et al., 2014; Liang et al., 2016; Vikraman et al., 2018; Wang et al., 2009; Yu et al., 2016), metal selenides (Gong et al., 2012; Lee and Lo, 2009), metal nitrides (Li et al., 2011; Xin et al., 2011), metal carbides (Jang et al., 2010; Lee et al., 2011) and metal tellurides (Hussain et al., 2018). Among these materials, transition metal sulfides have drawn much attention due to their bandgap tunability, interesting chemical behaviors, and adoptability of photoelectrochemical performance. Various research groups have previously explored the capability of metal sulfides (MoS_2, WS_2, CuS, etc.) and hybrid structures to improve the performance and catalytic activity of DSSCs such as $MoSe_2$/Mo (Hussain et al., 2017b), WSe_2/W (Hussain et al., 2017a), MoS_2 (Hussain et al., 2015b; Vikraman et al., 2018), WS_2 (Hussain et al., 2015a), CuS (Patil, Supriya A et al., 2017a,b; Sangamesha et al., 2013) multi-wall carbon nanotubes decorated on tungsten sulfide (MWCNTs-WS_2) (Yue et al., 2013), MoS_2 nanosheets coated onto multi-walled carbon nanotubes (MoS_2-MWCNTs) (Tai et al., 2012), and composites of MoS_2/graphene flakes (Yue et al., 2012) or MoS_2/graphene nanocomposite (Liu et al., 2012). To date, the maximum power conversion efficiencies (PCEs) using MoS_2

* Corresponding authors at: Graphene Research Institute, Sejong University, Seoul 143-747, Republic of Korea (J. Jung). Department of Mechanical Engineering, Hanyang University, Haengdang-dong, Seongdong-gu, 133-791 Seoul, Republic of Korea (H.-S. Kim).
E-mail addresses: kima@hanyang.ac.kr (H.-S. Kim), jwjung@sejong.ac.kr (J. Jung).
[1] Authors are equally contributed.

https://doi.org/10.1016/j.solener.2018.05.074
Received 27 February 2018; Received in revised form 2 May 2018; Accepted 21 May 2018

and WS_2 DSSCs were at ~7.59–7.69% and ~7.73%, respectively, which came close to the performance of the DSSC using a Pt CE (Al-Mamun et al., 2014; Wu et al., 2011). In addition, Congju et al., reported cobalt sulfide (CoS) CE using organic ink with the efficiency of 6.6% (Congiu et al., 2015) and a novel water based ink with the efficiency of 6.8% (Congju et al., 2016). In earlier, various research groups studied mesoporous p-type semiconductor and n-type semiconductor as a photoelectrodes for DSSCs (Cavallo et al., 2017). Bonomo et al., studied the limitation of CoS anode in DSSCs (Bonomo et al., 2017). In this work, to avoid harming the environment through a complex solution-based preparation process, the simple RF magnetron sputtering – chemical vapor deposition (CVD) process was used for the development of large area CuS/WS_2 and CuS/MoS_2 heterostructures onto conductive substrates.

The synthesized CuS/WS_2 and CuS/MoS_2 were employed as CEs in DSSCs. To the best of our knowledge, using CuS/WS_2 or CuS/MoS_2 heterostructure as the CE in DSSCs has not been reported. Two CEs possesses excellent electrocatalytic activity for I_3^- reduction and high electrochemical stability. The DSSCs assembled with CuS/WS_2 and CuS/MoS_2 CE achieved PCEs of 8.21% and 7.12%, respectively, under a simulated solar illumination of 100 mW cm^{-2} (AM 1.5), which are closer to that of 8.74% for the DSSC with Pt CE and higher than those of the DSSCs with pure WS_2, MoS_2, and CuS CE (6.3%, 6.6%, and 6.4%).

2. Experimental details

2.1. Synthesis of CuS/WS_2 and CuS/MoS_2

Initially, fluorine-doped tin oxide transparent (FTO) glass substrates were cleaned with acetone, ethanol, and deionized water and then baked at 120 °C for 5 min. After loading the FTO/glass substrates into a sputtering chamber, the chamber was evacuated by a rotary pump and a turbomolecular pump combination to a pressure of ~1×10^{-7} torr. The Mo and W films were deposited onto FTO/glass by sputtering system (Power = 100 W) at room temperature for 30 min using W and Mo target (99% pure). Subsequently, the deposited Mo or W film was further annealed in sulfurization at 500 °C to form MoS_2 or WS_2 film. After that, Cu film was deposited on it by sputtering as well. Then, the Cu/MoS_2 and Cu/WS_2 films were sulfurized again at 500 °C to produce (CuS/WS_2 & CuS/MoS_2) heterostructure. In sputtering system target to substrate distance (50 mm), gas flow (10 sccm) and working pressure (~2×10^{-3} torr) were fixed. CVD growth conditions such as weight of sulfur powder (0.4 g), distance between the boat and substrate (~50 mm) and working pressure (~2×10^{-1} torr) were constantly maintained for all the experiments.

2.2. Fabrication of DSSCs and their measurement

The Pt-coated CEs were prepared by spreading a 2 mM chloroplatinic acid hexahydrate (H_2PtCl_6) drop in isopropanol onto the FTO substrates and heating it to 400 °C for 15 min under ambient air. The polymer electrolyte was prepared using 0.1 M LiI, 0.6 M 1-propyl-2,3-dimethylimidazolium iodide, 0.05 M I_2, 0.5 M 4-tert-buylpyridine, and 3% w/w polyethylene oxide (M_w 3000,000) with 5 ml acetonitrile as a solvent (Memon et al., 2017a, 2017b).

For TiO_2 photo anode fabrication, FTO substrates at a size of 1.5 cm × 1.5 cm were ultrasonically cleaned sequentially in acetone, deionized water, and ethanol. The anatase TiO_2 (P25) and rutile TiO_2 (G2) pastes were prepared by our previously reported method (Patil et al., 2014; Patil, Supriya A. et al., 2017a,b). P25 and G2 were deposited on the FTO glass by double masking tape with a thickness of 18 μm. The FTO-coated photo anodes were initially dried at 70 °C for 30 min followed by high temperature sintering with a consecutive temperature sequence of 125, 325, 375, 450, and 500 °C for 6, 5, 5, 15, and 15 min, respectively, using a furnace. Also, $TiCl_4$ treatment was carried out before and after deposition of the paste onto the FTO. The sintered photo anodes were immersed in a 0.3 mM N719 dye solution for 12 h. The DSSCs were fabricated by sandwiching the dye-immersed TiO_2 photo anodes with an active area of 0.20 cm^2 and MoS_2/CuS, WS_2/CuS, or Pt based CEs with a 60 μm-thick surlyn as a sealant cell spacer. A 3% gel electrolyte was filled into the cell through a hole drilled into the photo anodes.

A solar simulator (150-W Xe lamp, Sun 2000 solar simulator, ABET 5 Technologies, USA) equipped with an AM 1.5G filter was used to generate simulated sunlight with a corrected intensity of 100 mW cm^{-2}. The current – voltage (*J-V*) spectra of DSSCs with different MoS_2-CuS/FTO, WS_2-CuS/FTO, and Pt/FTO CEs were obtained using a Keithley 2400 source meter. Cyclic voltammetry (CV) measurements were performed using a three-electrode system (Bio Logic Co.) at a scan rate of 10 mV s^{-1}. Electrochemical impedance spectra (EIS) were obtained using CompactStat (IviumStat Technologies, The Netherlands) in the frequency range of 100 kHz to 0.1 Hz. For the EIS and polarization measurements, the symmetrical dummy cells were assembled with two identical CEs filled with the same electrolyte used in the DSSCs.

3. Results and discussion

The preparation scheme for the fabrication of CuS/WS_2 and CuS/MoS_2 CEs by sputtering- CVD is displayed in Fig. 1a–c. Initially, for the fabrication of WS_2 and MoS_2 films, W and Mo seeds were deposited by RF sputtering onto the FTO substrate and were then subjected to a

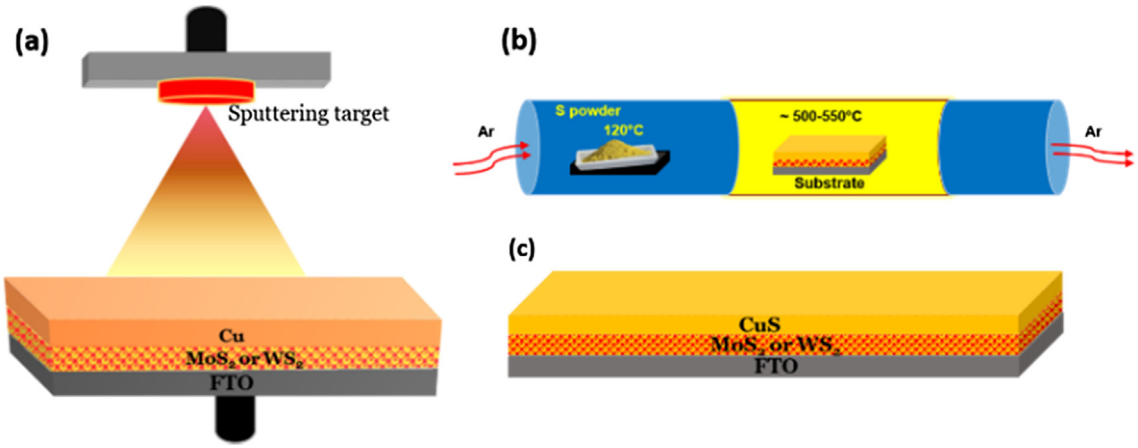

Fig. 1. Schematic of CuS/WS_2 and CuS/MoS_2 synthesis. (a) Copper (Cu) deposition on the top of WS_2/FTO or MoS_2/FTO film. (b) CuS/WS_2 and CuS/MoS_2 heterostructure formation by sulfurization process. (c) Structure of CuS/WS_2 or MoS_2/FTO.

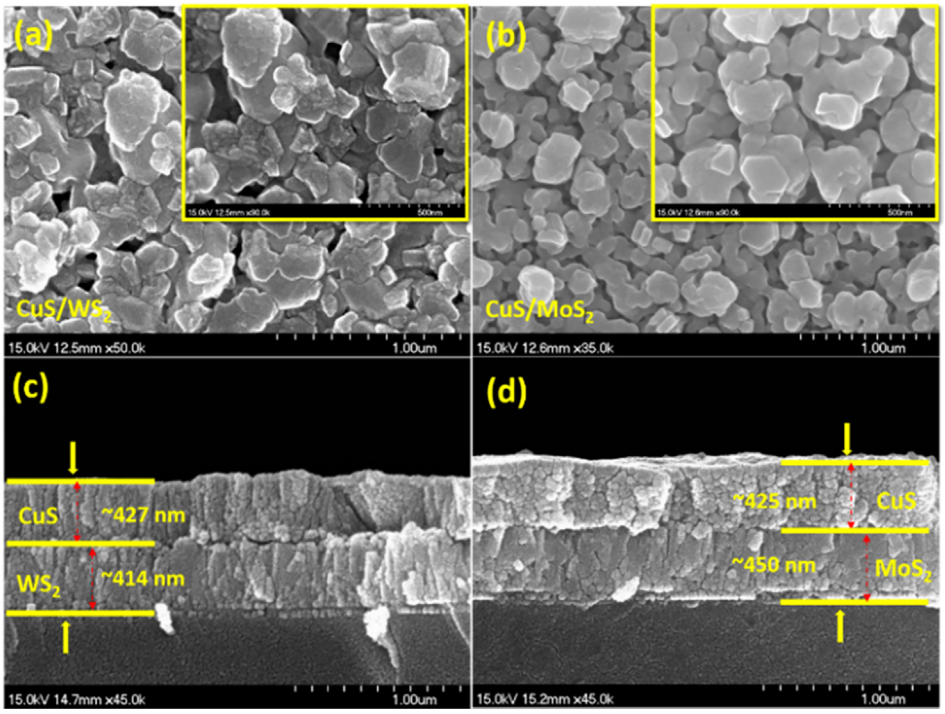

Fig. 2. (a–b) Surface and (c–d) cross-sectional FESEM images of CuS/WS_2 and CuS/MoS_2.

sulfurization process. A thin Cu layer was then deposited onto the MoS_2/FTO and WS_2/FTO (Fig. 1a). The prepared Cu/WS_2 and Cu/MoS_2 layers were converted to CuS/WS_2 and CuS/MoS_2 by sulfurization process using CVD (Fig. 1b). The schematic of the CuS/WS_2 and MoS_2/FTO is shown in Fig. 1c.

Field emission scanning electron microscopy (FE-SEM) was used to study the surface morphology and cross-sectional view of CuS/WS_2 and CuS/MoS_2 heterostructure. From the SEM images shown in Fig. 2a and b, the films are uniformly covered with different sized grains with porous structure which allows the formation of an electrolyte-electrode interface and hence improve the electrocatalytic activity for the I^-/I_3^- redox reaction. However, the CuS/WS_2 heterostructure exhibits larger sized grains compared to CuS/MoS_2 of around ~150–200 nm. Larger sized grains are formed by the agglomerations of smaller grains for CuS/WS_2 as shown in the inset of Fig. 2a. The cross-sectional-FESEM images (Fig. 2c and d) confirm the presence of the bilayer nature of CuS/WS_2 (~414 nm WS_2 and ~427 nm CuS) and CuS/MoS_2 (~450 nm MoS_2 and ~425 nm CuS) heterostructures.

The energy dispersive X-ray spectroscopy (EDX) spectrum of the CuS/WS_2 and CuS/MoS_2 signifies their individual elements as shown in Figs. S1 and S2, respectively. The EDX mapping images are provided for CuS/WS_2 (Cu, S, W, Sn, and O elements) and CuS/MoS_2 heterostructure (Cu, S, Mo, Sn, and O elements) in the supporting information (Figs. S3 and S4, respectively). From Figs. S3 and S4, W, S, and Cu (CuS/WS_2), and Mo, S, and Cu (CuS/MoS_2) elements are indeed present and spatially distributed across the entire surface of the films, which confirms the purity of the heterostructure.

The structural analysis was ascertained by Raman scattering for CuS, WS_2, MoS_2, CuS/WS_2, and CuS/MoS_2 films. From the spectra of Fig. 3a, the WS_2 characteristic peaks appear at ~354.2 cm^{-1} and ~418.4 cm^{-1}, corresponding to the in-plane vibration of W and sulfur atoms, E^1_{2g} mode and the out-of-plane vibration of sulfur atoms, A_{1g} mode, respectively (Zeng et al., 2013). The CuS spectrum reveals a pronounced peak at 474.1 cm^{-1}, which contributes to the vibrational (stretching) mode of the covalent S—S bond and a weaker broadened peak at about 270.5 cm^{-1} attributed to the Cu—S bond vibration (Ishii et al., 1993; Milekhin et al., 2015). From Fig. 3b, CuS exhibits characteristic peaks and the MoS_2 atomic layer spectrum contains characteristic peaks at ~381.2 cm^{-1} and 408.1 cm^{-1}, corresponding to the in-plane E^1_{2g} mode and the out-of-plane A_{1g} mode, respectively (Vikraman et al., 2017; Yang et al., 2014). In the case of CuS/WS_2 and CuS/MoS_2 heterostructures (Fig. 3a and b), CuS characteristic peaks co-exist with WS_2 and MoS_2 peaks with only slight variations in their intensity.

X-ray diffraction (XRD) analysis was carried out to reveal the structure of WS_2, MoS_2, CuS/WS_2 and CuS/MoS_2 films as shown in Fig. 3c–d. The observed XRD patterns are well consistent with standard patterns (JCPDS No.: WS_2 - 872417, MoS_2 - 872,416 & CuS - 782121) for the hexagonal phase primitive lattice structures of WS_2, MoS_2, and CuS. In the case of CuS/WS_2 and CuS/MoS_2, the CuS related peaks are dominant due to their top position in the heterostructure. In addition, the conventional peak of (0 0 2) lattice orientation for the layered structure of MoS_2 and WS_2 appears in the XRD pattern of heterostructures. No other impurity peaks or different phase oriented peaks are observed for either heterostructure.

X-ray photoemission spectroscopy (XPS) was used to probe the chemical compositions of the CuS/WS_2 and CuS/MoS_2 heterostructures. The XPS spectra display the Mo, S, and Cu binding energies (Fig. 4a–c), for the CuS/MoS_2 heterostructure. The spectra reveal the existence of Mo^{4+} peaks at 229.2 eV ($3d_{5/2}$) and 232.1 eV ($3d_{3/2}$), and S^{2-} peaks at 162.3 eV ($2p_{3/2}$) and 163.5 eV ($2p_{1/2}$) (Brown et al., 1998; Liu et al., 2014; Wang et al., 2015). Two more peaks appeared at 932.4 eV (Cu $2p_{3/2}$) and 952.5 eV (Cu $2p_{1/2}$) from Cu (Natarajan Karikalan et al., 2017). Fig. 4d–f shows the XPS spectra of W 4f, S 2p, and Cu 2p binding energies for the CuS/WS_2 heterostructure. The W4f core peaks appear at 34.7, and 32.4 eV, which correspond to the W $4f_{5/2}$ and W $4f_{7/2}$ levels for W^{4+}, respectively. The S 2p core-level spectrum reveals peaks at 163.5 and 162.4 eV, which corresponds to the S $2p_{1/2}$ and S $2p_{3/2}$ state, respectively (Park et al., 2015; Song et al., 2013). The Cu 2p spectrum (Fig. 4f) reveals two Cu 2p peaks at 932.4 and 952.6 eV which represent Cu $2p_{3/2}$ and Cu $2p_{1/2}$, respectively (Tanveer et al., 2014).

To evaluate the reaction kinetics and electrocatalytic activities of CuS/WS_2, CuS/MoS_2, and Pt, cyclic voltammetry (CV) analysis was performed using three electrode system using Ag/AgCl as a reference

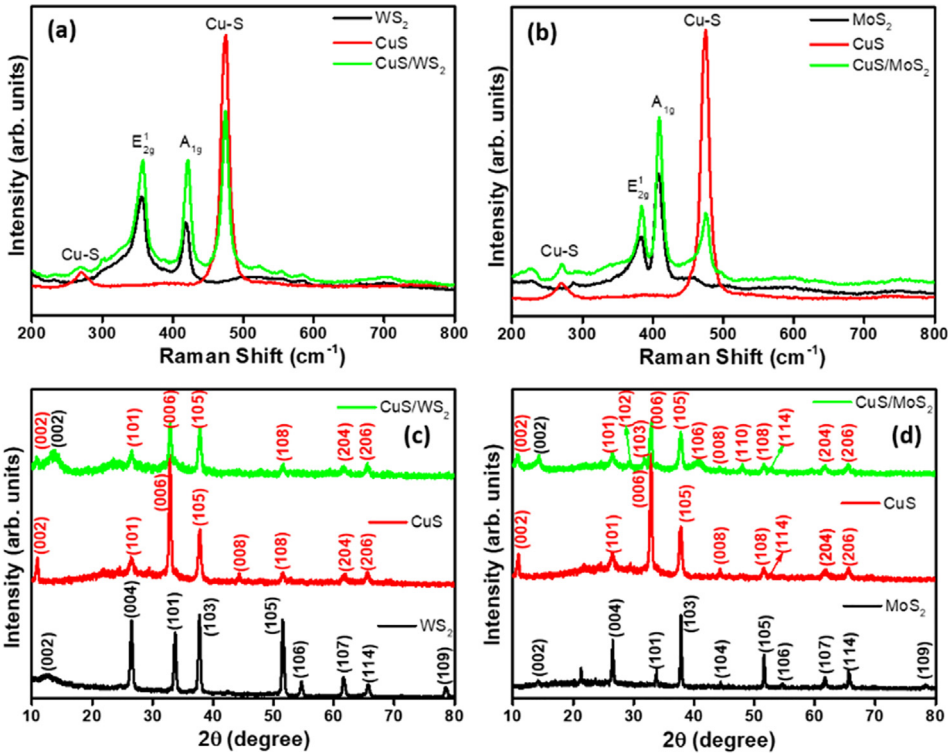

Fig. 3. Raman and XRD spectra: (a, c) WS_2, CuS, and CuS/WS_2 heterostructures (XRD peaks are indexed with black for WS_2 and red for CuS) and (b, d) MoS_2, CuS, and CuS/MoS_2 heterostructures (XRD peaks are indexed with black for MoS_2 and red for CuS).

electrode, Pt wire as a CE, and the prepared samples as working electrodes in an acetonitrile solution consisting of 10 mM LiI, 1 mM I_2, and 0.1 mM $LiClO_4$ at a scan rate of 10 mV s^{-1}. Fig. 5a shows the CV curves for Pt, CuS/WS_2, and CuS/MoS_2 in the potential interval between −0.2 and 1.0 V vs. Ag/AgCl. CV curves show two redox peaks which correspond to the reduction of I_3^- (anodic peak, Red-1 and Red-2) and the oxidation of I^- (cathodic peak, Ox-1 and Ox-2). The anodic and cathodic peaks are the key features for electrocatalytic activity because they are obvious evidence representing the reduction of I_3^- to I^- (Hu et al., 2015). The oxidation and reduction peak of I_3^-/I^- for the CuS/WS_2 and CuS/MoS_2 heterostructures were almost identical to Pt, suggesting that they are effective in catalyzing the reduction of I_3^- to I^-. The cathode peak current (I_{pc}) at the I^-/I_3^- reduction, cathodic peak potential (E_{pc}), and peak-to-peak separation (between anodic and cathodic peaks, E_{pp}) are important parameters for determining the electrochemical catalytic activity of CEs. The E_{pp} is inversely correlated

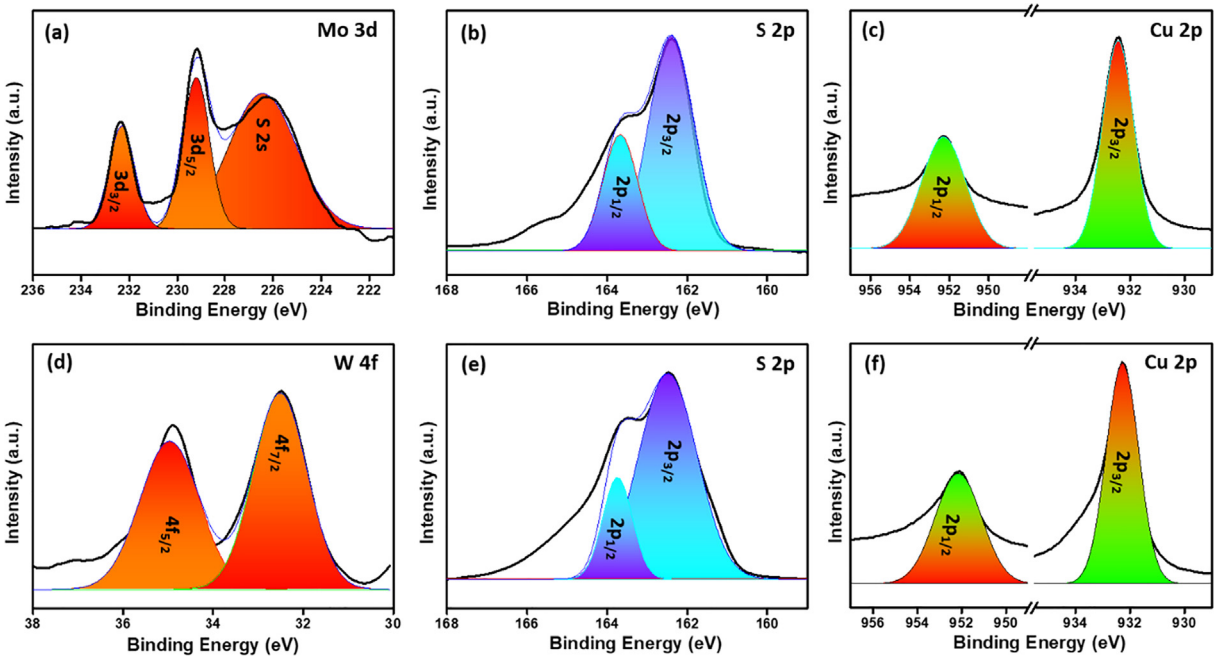

Fig. 4. XPS spectra: (a–c) Mo, S, and Cu element binding energies for the CuS/MoS_2 heterostructure. (d–f) W, S, and Cu element binding energies for the CuS/WS_2 heterostructure.

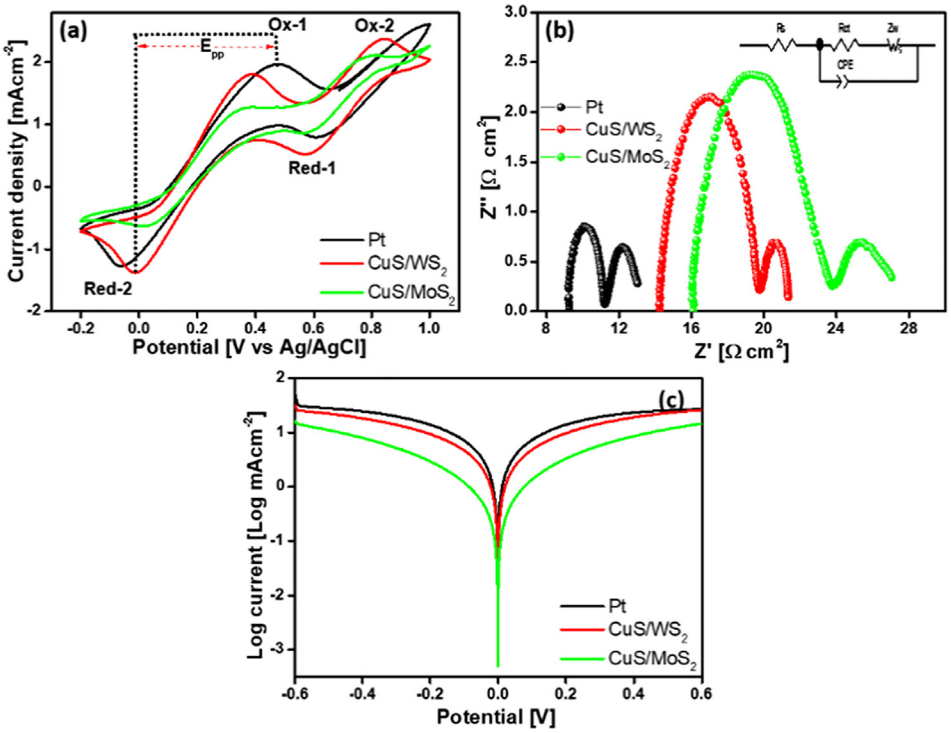

Fig. 5. (a) CV curves of different CEs at a scan rate of 10 mV s^{-1}; (b) Nyquist plots of the symmetrical cells; Inset – equivalent circuit of symmetrical cell (R_{ct}: charge transfer resistance, Z_w: diffusion impedance, R_s: ohmic internal resistance, CPE: constant phase element); (c) Tafel polarization curves of symmetrical cells.

with the electrochemical rate constant of the redox reaction peaks, k_s ($E_{pp} \propto 1/k_s$). Higher I_{pc}, more positive E_{pc}, and lower E_{pp} values provide a better electrocatalytic activity of CE for the reduction of I_3^- ions in the corresponding DSSCs. The observed values of I_{pc} are 1.96, 1.80, and 1.26 mA cm^{-2}, and E_{pp} values are 533, 398, and 332 mV for Pt, CuS/WS_2, and CuS/MoS_2, respectively. Notably, the Red-2 peak for the CuS/WS_2 is shifted towards positive potential compared to those for Pt CEs, suggesting that there are lower overpotential losses in heterostructure CEs as well as better electrocatalytic activity and faster reaction velocity for I_3^- reduction. Furthermore, the current densities of the redox peaks for CuS/WS_2 CE are much higher than those of CuS/MoS_2 CE, which can be ascribed to the larger specific surface area due to the formation of smaller sized grains as described in the SEM section earlier (Fig. 2a), which promotes electrocatalytic activity. Furthermore, it is believed that the catalytic active sites of the TMDC material lie on the surface morphology and the active edge sites which are located on the edges layered material (Lei et al., 2014; Zhang et al., 2014).

CV curves of CuS/WS_2 CE were measured at different scan rates ranging from 10 to 100 mV s^{-1} (Fig. S5). The cathodic peak currents shift towards positively and their anodic peaks shift towards negatively as the scan rate increases, which suggests that the inner sites of the CEs also become more reactive and possess catalytic activity at a higher scan rate (Kung et al., 2012; Yue et al., 2012).

Electrochemical stability is also a key concern for practical DSSC application. For this purpose, electrochemical stability of the CEs (CuS/WS_2 and CuS/MoS_2) was analyzed by subjecting 50 consecutive cycles of CV measurements for I^-/I_3^- reduction at a scan rate of 10 mV s^{-1} (Fig. S6a-b). No drastic variation in CV curve shape or peak current densities from 1 to 50 cycles for both (CuS/WS_2 and CuS/MoS_2) CEs were observed. From the stability curves, it is clear that the fabricated CEs possess good electrochemical activity in I^-/I_3^- electrolytes, superior electrochemical stability, and strong adhesion to the FTO substrate.

Electrochemical impedance spectroscopy (EIS) was used to investigate the internal resistance and electrode kinetics of symmetric cells fabricated with two identical electrodes (CE/electrolyte/CE) at a frequency range from 0.1 to 100 kHz. The corresponding Nyquist plots of Pt, CuS/WS_2, and CuS/MoS_2 are shown in Fig. 5b. The high-frequency intercept on the real axis is associated with the intrinsic ohmic series resistance (R_s) of the electrolyte and electrodes, the diameter of high-frequency semicircle R_{ct} is the charge-transfer resistance at the electrolyte-electrode interface, and the low frequency semicircle corresponds to the Nernst diffusion impedance (Z_w) of the I^-/I_3^- redox couple in the electrolyte. It is noticed that the values of R_s (14.80 & 16.78 Ω cm^2) for CuS/WS_2 and CuS/MoS_2 CEs are similar, but higher than that of the Pt CE (9.35 Ω cm^2) due to their semiconducting behavior (Han et al., 2005; Koide et al., 2006). R_s indicates electron-conducting ability (Dong et al., 2015), affects the fill factor, and the performance of DSSCs (Joshi et al., 2010).

The R_{ct} of Pt and CuS/WS_2 CE (3.66 & 6.53 Ω cm^2) is smaller than that of CuS/MoS_2 CEs (10.26 Ω cm^2), manifesting the higher electrocatalytic reduction of I_3^- which could enhance the FF of DSSCs (Ramasamy et al., 2008). R_s and R_{ct} values are in order of Pt < CuS/WS_2 < CuS/MoS_2, which are in a good agreement with J_{sc} and FF values as discussed later.

The anodic and cathodic branches of the Tafel curve provide information about the exchange current density (J_0) (Fig. 5c). Based on the tangent slope of the Tafel curves, J_0 values for the fabricated dummy cells are in order of Pt > CuS/WS_2 > CuS/MoS_2. The CuS/WS_2 sample exhibits higher cathodic peak current than CuS/MoS_2 and higher electrocatalytic ability towards I^-/I_3^- redox couples. Furthermore, J_0 can be calculated using Eq. (1),

$$J_0 = \frac{RT}{nFR_{ct}} \tag{1}$$

where R is the gas constant, T is the temperature (298 K), F is Faraday's constant, n is the number of electrons involved in the I_3^- reduction reaction, and R_{ct} is the charge transfer resistance obtained from the EIS spectrum. A higher J_0 for Pt and CuS/WS_2 CEs contributes to lower values of R_{ct} in the impedance measurement.

The schematic representation of DSSCs with CuS/WS_2 and CuS/MoS_2 CEs are illustrated in Fig. 6a. The photocurrent–voltage (*J-V*)

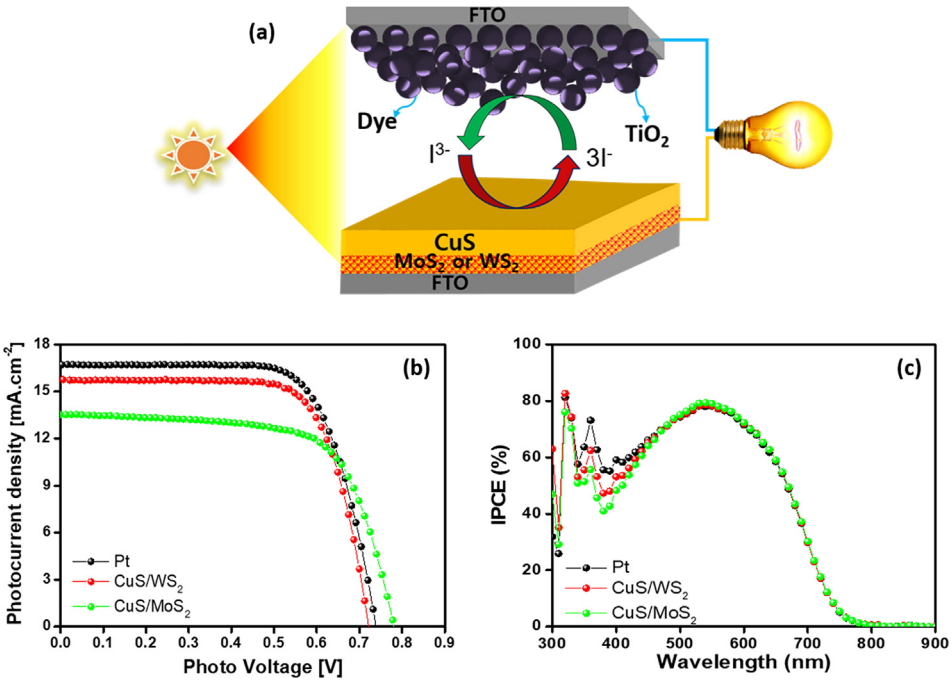

Fig. 6. (a) Schematic representation of the electrocatalytic mechanism in DSSCs using Pt, CuS/MoS_2, and CuS/WS_2 heterostructure CEs; (b–c) Photocurrent–voltage and IPCE curves of DSSCs with different CEs, measured at AM 1.5G illumination (100 mW cm^{-2}).

Table 1
Photovoltaic and EIS parameters of Pt, CuS/WS_2, and CuS/MoS_2 based DSSC CEs.

Type of CE	V_{oc} (V)	Jsc (mA cm^{-2})	FF (%)	PCE η (%)	Rs (Ω cm^2)	Rct (Ω cm^2)
Pt	0.73	16.71	70.78	8.74	9.35	3.66
CuS/WS_2	0.72	15.77	72.16	8.21	14.80	6.53
CuS/MoS_2	0.78	13.52	67.49	7.21	16.78	10.26

curves of the DSSCs with Pt, CuS/WS_2, and CuS/MoS_2 CEs were measured under a simulated solar illumination of 100 mW cm^{-2} (AM 1.5) (Fig. 6b). The photovoltaic parameters of DSSCs such as short-circuit photocurrent density (J_{sc}), open circuit voltage (V_{oc}), fill factor (FF), and PCE are listed in Table 1. The DSSC with CuS/WS_2 CE yielded a remarkable PCE of 8.21% (J_{sc} = 15.77 mA cm^{-2}, V_{oc} = 0.72 V, FF = 72.16), while the DSSC with CuS/MoS_2 CE produced a PCE of 7.12% (J_{sc} = 13.52 mA cm^{-2}, V_{oc} = 0.78 V, FF = 67.49). For reference, the Pt-coated CE-based DSSC, measured under the same condition, gave a PCE of 8.74% (J_{sc} = 16.71 mA cm^{-2}, V_{oc} = 0.73 V, FF = 70.78). For the repeatability test of DSSC devices, we prepared five DSSCs using different CuS/WS_2 and CuS/MoS_2 CEs and their performances are provided in the supporting information Figs. S7 and S8, respectively. Pure WS_2, MoS_2, and CuS films exhibited inferior PCEs of 6.0%, 6.3%, and 6.4%, respectively (Fig. S9 and Table S1) (Hussain et al., 2015a, 2015b). In comparison, PCEs of 6.42%, 5.82%, and 5.72%, respectively were obtained for the DSSCs by adopting Co-S, Mo-S, and Ni-S CE, respectively (Huang et al., 2016). The enhancement in FF value for the DSSC based on the CuS/WS_2 CE, as compared to CuS/MoS_2, WS_2, MoS_2, and CuS, can be attributed to its low R_s and R_{ct} values (Han et al., 2005; Koide et al., 2006). In addition, close contact between the WS_2 or MoS_2 and CuS promotes electron flow between the WS_2 or MoS_2 and CuS, and improves J_{sc} value, and increases the total current of the I^-/I_3^- redox reaction (Papageorgiou et al., 1997; Yoon et al., 2008). Fig. 6c shows the incident photon to current conversion efficiency (IPCE) curves of DSSCs for CuS/WS_2, CuS/MoS_2, and Pt CEs.

Moreover, CE with higher thickness (~517 nm) of the top layer of CuS on WS_2 film (Fig. S10a) exhibited a lower PCE (7.7%) as shown in Fig. S10b. This deterioration might be attributed to the blocking of electrolyte penetration into the heterostructure due to the thick top layer, which is not beneficial for the transfer of electrons between WS_2 and CuS (Al-Mamun et al., 2014).

4. Conclusions

In summary, CuS/WS_2 and CuS/ MoS_2 heterostructures were successfully synthesized by CVD-sputtering process and these were utilized as CE in DSSCs. The CV and EIS measurements of CuS/WS_2 and CuS/MoS_2 heterostructures revealed the low charge transfer resistance at the electrolyte–electrode interface, good electrocatalytic activity, and fast reaction kinetics for the I^-/I_3^- redox reaction as well as high electrochemical stability with no significant sign of degradation after 50 consecutive CV cycles. CuS/WS_2 and CuS/ MoS_2 CEs achieved high PCEs of 8.21% and 7.12%, respectively, under a simulated solar illumination of 100 mW cm^{-2} (AM 1.5). The proposed heterostructure would be a suitable potential CE to replace Pt for highly efficient DSSCs.

Acknowledgments

This research was supported by the Basic Science Research Program through the National Research Foundation of Korea (NRF), funded by the Ministry of Education (2010-0020207, 2016R1D1A1B01015047, 2017R1C1B5076952, 2018044021), by the MOTIE (10052928) and KSRC (Korea Semiconductor Research Consortium) support programs for the development of future semiconductor devices, and by the Nano Material Technology Development Program through the National Research Foundation of Korea (NRF) funded by the Ministry of Science, ICT, and Future Planning (2015 M3A7B7045194, 2016

M3A7B4909942).

Appendix A. Supplementary material

Supplementary data associated with this article can be found, in the online version, at http://dx.doi.org/10.1016/j.solener.2018.05.074.

References

Al-Mamun, M., Zhang, H., Liu, P., Wang, Y., Cao, J., Zhao, H., 2014. Directly hydrothermal growth of ultrathin MoS 2 nanostructured films as high performance counter electrodes for dye-sensitised solar cells. RSC Adv. 4 (41), 21277–21283.

Bi, E., Chen, H., Yang, X., Peng, W., Grätzel, M., Han, L., 2014. A quasi core–shell nitrogen-doped graphene/cobalt sulfide conductive catalyst for highly efficient dye-sensitized solar cells. Energy Environ. Sci. 7 (8), 2637–2641.

Bonomo, M., Congiu, M., De Marco, M.L., Dowling, D.P., Di Carlo, A., Graeff, C.F., Dini, D., 2017. Limits on the use of cobalt sulfide as anode of p-type dye-sensitized solar cells. J. Phys. D Appl. Phys. 50 (21), 215501.

Brown, N.M., Cui, N., McKinley, A., 1998. An XPS study of the surface modification of natural MoS 2 following treatment in an RF-oxygen plasma. Appl. Surf. Sci. 134 (1), 11–21.

Cavallo, C., Di Pascasio, F., Latini, A., Bonomo, M., Dini, D., 2017. Nanostructured semiconductor materials for dye-sensitized solar cells. J. Nanomater. 2017.

Congiu, M., Bonomo, M., Marco, M.L.D., Dowling, D.P., Di Carlo, A., Dini, D., Graeff, C.F., 2016. Cobalt sulfide as counter electrode in p-type dye-sensitized solar cells. ChemistrySelect 1 (11), 2808–2815.

Congiu, M., Lanuti, A., di Carlo, A., Graeff, C.F., 2015. A novel and large area suitable water-based ink for the deposition of cobalt sulfide films for solar energy conversion with iodine-free electrolytes. Sol. Energy 122, 87–96.

Dong, J., Wu, J., Jia, J., Wu, S., Zhou, P., Tu, Y., Lan, Z., 2015. Cobalt selenide nanorods used as a high efficient counter electrode for dye-sensitized solar cells. Electrochim. Acta 168, 69–75.

Gong, F., Wang, H., Xu, X., Zhou, G., Wang, Z.-S., 2012. In situ growth of Co0. 85Se and Ni0. 85Se on conductive substrates as high-performance counter electrodes for dye-sensitized solar cells. J. Am. Chem. Soc. 134 (26), 10953–10958.

Grätzel, M., 2001. Photoelectrochemical cells. Nature 414 (6861), 338–344.

Han, L., Koide, N., Chiba, Y., Islam, A., Komiya, R., Fuke, N., Fukui, A., Yamanaka, R., 2005. Improvement of efficiency of dye-sensitized solar cells by reduction of internal resistance. Appl. Phys. Lett. 86 (21), 213501.

Hu, Z., Xia, K., Zhang, J., Hu, Z., Zhu, Y., 2015. Highly transparent ultrathin metal sulfide films as efficient counter electrodes for bifacial dye-sensitized solar cells. Electrochim. Acta 170, 39–47.

Huang, N., Zheng, F., Xu, J., Huang, H., Li, G., Xia, Z., Sun, P., Sun, X., 2016. Solution-based in–situ synthesis of transition metal sulfides as efficient counter electrodes for dye-sensitized solar cells. ChemistrySelect 1 (15), 4613–4619.

Hussain, S., Patil, S.A., Vikraman, D., Arbab, A.A., Jeong, S.H., Kim, H.-S., Jung, J., 2017a. Growth of a WSe_2/W counter electrode by sputtering and selenization annealing for high-efficiency dye-sensitized solar cells. Appl. Surf. Sci. 406, 84–90.

Hussain, S., Patil, S.A., Vikraman, D., Liu, H., Kim, H.-S., Jung, J., 2017b. High performance $MoSe_2$/Mo counter electrodes based-dye-sensitized solar cells. J. Electrochem. Soc. 164 (2), E11–E16.

Hussain, S., Patil, S.A., Vikraman, D., Mengal, N., Liu, H., Song, W., An, K.-S., Jeong, S.H., Kim, H.-S., Jung, J., 2018. Large area growth of MoTe 2 films as high performance counter electrodes for dye-sensitized solar cells. Sci. Rep. 8 (1), 29.

Hussain, S., Shaikh, S.F., Vikraman, D., Mane, R.S., Joo, O.-S., Naushad, M., Jung, J., 2015a. Sputtering and sulfurization-combined synthesis of a transparent WS_2 counter electrode and its application to dye-sensitized solar cells. RSC Adv. 5 (125), 103567–103572.

Hussain, S., Shaikh, S.F., Vikraman, D., Mane, R.S., Joo, O.S., Naushad, M., Jung, J., 2015b. High-performance platinum-free dye-sensitized solar cells with molybdenum disulfide films as counter electrodes. ChemPhysChem 16 (18), 3959–3965.

Ishii, M., Shibata, K., Nozaki, H., 1993. Anion distributions and phase transitions in CuS1-xSex (x= 0–1) studied by Raman spectroscopy. J. Solid State Chem. 105 (2), 504–511.

Jang, J.S., Ham, D.J., Ramasamy, E., Lee, J., Lee, J.S., 2010. Platinum-free tungsten carbides as an efficient counter electrode for dye sensitized solar cells. Chem. Commun. 46 (45), 8600–8602.

Joshi, P., Zhang, L., Chen, Q., Galipeau, D., Fong, H., Qiao, Q., 2010. Electrospun carbon nanofibers as low-cost counter electrode for dye-sensitized solar cells. ACS Appl. Mater. Interfaces 2 (12), 3572–3577.

Koide, N., Islam, A., Chiba, Y., Han, L., 2006. Improvement of efficiency of dye-sensitized solar cells based on analysis of equivalent circuit. J. Photochem. Photobiol., A 182 (3), 296–305.

Kung, C.-W., Chen, H.-W., Lin, C.-Y., Huang, K.-C., Vittal, R., Ho, K.-C., 2012. CoS acicular nanorod arrays for the counter electrode of an efficient dye-sensitized solar cell. ACS Nano 6 (8), 7016–7025.

Lee, K.S., Lee, W.J., Park, N.-G., Kim, S.O., Park, J.H., 2011. Transferred vertically aligned N-doped carbon nanotube arrays: use in dye-sensitized solar cells as counter electrodes. Chem. Commun. 47 (14), 4264–4266.

Lee, Y.L., Lo, Y.S., 2009. Highly efficient quantum-dot-sensitized solar cell based on co-sensitization of CdS/CdSe. Adv. Funct. Mater. 19 (4), 604–609.

Lei, B., Li, G., Gao, X., 2014. Morphology dependence of molybdenum disulfide transparent counter electrode in dye-sensitized solar cells. J. Mater. Chem. A 2 (11), 3919–3925.

Li, G., Song, J., Pan, G., Gao, X., 2011. Highly Pt-like electrocatalytic activity of transition metal nitrides for dye-sensitized solar cells. Energy Environ. Sci. 4 (5), 1680–1683.

Liang, J., Li, J., Zhu, H., Han, Y., Wang, Y., Wang, C., Jin, Z., Zhang, G., Liu, J., 2016. One-step fabrication of large-area ultrathin MoS 2 nanofilms with high catalytic activity for photovoltaic devices. Nanoscale 8 (35), 16017–16025.

Liu, C.-J., Tai, S.-Y., Chou, S.-W., Yu, Y.-C., Chang, K.-D., Wang, S., Chien, F.S.-S., Lin, J.-Y., Lin, T.-W., 2012. Facile synthesis of MoS 2/graphene nanocomposite with high catalytic activity toward triiodide reduction in dye-sensitized solar cells. J. Mater. Chem. 22 (39), 21057–21064.

Liu, N., Kim, P., Kim, J.H., Ye, J.H., Kim, S., Lee, C.J., 2014. Large-area atomically thin MoS_2 nanosheets prepared using electrochemical exfoliation. ACS Nano 8 (7), 6902–6910.

Memon, A.A., Arbab, A.A., Sahito, I.A., Mengal, N., Sun, K.C., Qadir, M.B., Choi, Y.S., Jeong, S.H., 2017a. Facile fabrication of activated charcoal decorated functionalized multi-walled carbon nanotube electro-catalyst for high performance quasi-solid state dye-sensitized solar cells. Electrochim. Acta 234 (Supplement C), 53–62.

Memon, A.A., Arbab, A.A., Sahito, I.A., Sun, K.C., Mengal, N., Jeong, S.H., 2017b. Synthesis of highly photo-catalytic and electro-catalytic active textile structured carbon electrode and its application in DSSCs. Sol. Energy 150 (Supplement C), 521–531.

Milekhin, A.G., Yeryukov, N.A., Sveshnikova, L.L., Duda, T.A., Rodyakina, E.E., Gridchin, V.A., Sheremet, E.S., Zahn, D.R., 2015. Combination of surface-and interference-enhanced Raman scattering by CuS nanocrystals on nanopatterned Au structures. Beilstein J. Nanotechnol. 6, 749.

Natarajan Karikalan, R.K., Chen, S.-M., Karuppiah, C., Elangovan, A., 2017. Sonochemical synthesis of sulfur doped reduced graphene oxide supported CuS nanoparticles for the non-enzymatic glucose sensor applications. Sci. Rep. 7.

O'regan, B., Grätzel, M., 1991. A low-cost, high-efficiency solar cell based on dye-sensitized colloidal TiO2 films. Nature 353 (6346), 737–740.

Papageorgiou, N., Maier, W., Grätzel, M., 1997. An iodine/triiodide reduction electrocatalyst for aqueous and organic media. J. Electrochem. Soc. 144 (3), 876–884.

Park, J., Lee, W., Choi, T., Hwang, S.-H., Myoung, J.M., Jung, J.-H., Kim, S.-H., Kim, H., 2015. Layer-modulated synthesis of uniform tungsten disulfide nanosheet using gas-phase precursors. Nanoscale 7 (4), 1308–1313.

Patil, S.A., Kalode, P.Y., Mane, R.S., Shinde, D.V., Doyoung, A., Keumnam, C., Sung, M.M., Ambade, S.B., Han, S.-H., 2014. Highly efficient and stable DSSCs of wet-chemically synthesized MoS2 counter electrode. Dalton Trans. 43 (14), 5256–5259.

Patil, S.A., Mengal, N., Memon, A.A., Jeong, S.H., Kim, H.-S., 2017. CuS thin film grown using the one pot, solution-process method for dye-sensitized solar cell applications. J. Alloys Compd. 708 (Supplement C), 568–574.

Ramasamy, E., Lee, W.J., Lee, D.Y., Song, J.S., 2008. Spray coated multi-wall carbon nanotube counter electrode for tri-iodide reduction in dye-sensitized solar cells. Electrochem. Commun. 10 (7), 1087–1089.

Sangamesha, M., Pushpalatha, K., Shekar, G., Shamsundar, S., 2013. Preparation and characterization of nanocrystalline CuS thin films for dye-sensitized solar cells. ISRN Nanomater. 2013.

Song, J.-G., Park, J., Lee, W., Choi, T., Jung, H., Lee, C.W., Hwang, S.-H., Myoung, J.M., Jung, J.-H., Kim, S.-H., 2013. Layer-controlled, wafer-scale, and conformal synthesis of tungsten disulfide nanosheets using atomic layer deposition. ACS Nano 7 (12), 11333–11340.

Tai, S.-Y., Liu, C.-J., Chou, S.-W., Chien, F.S.-S., Lin, J.-Y., Lin, T.-W., 2012. Few-layer MoS 2 nanosheets coated onto multi-walled carbon nanotubes as a low-cost and highly electrocatalytic counter electrode for dye-sensitized solar cells. J. Mater. Chem. 22 (47), 24753–24759.

Tanveer, M., Cao, C., Aslam, I., Ali, Z., Idrees, F., Tahir, M., Khan, W.S., Butt, F.K., Mahmood, A., 2014. Effect of the morphology of CuS upon the photocatalytic degradation of organic dyes. RSC Adv. 4 (108), 63447–63456.

Vikraman, D., Akbar, K., Hussain, S., Yoo, G., Jang, J.-Y., Chun, S.-H., Jung, J., Park, H.J., 2017. Direct synthesis of thickness-tunable MoS_2 quantum dot thin layers: Optical, structural and electrical properties and their application to hydrogen evolution. Nano Energy 35, 101–114.

Vikraman, D., Patil, S.A., Hussain, S., Mengal, N., Kim, H.-S., Jeong, S.H., Jung, J., Kim, H.-S., Park, H.J., 2018. Facile and cost-effective methodology to fabricate MoS_2 counter electrode for efficient dye-sensitized solar cells. Dyes Pigm. 151, 7–14.

Wang, J., Chen, L., Lu, W., Zeng, M., Tan, L., Ren, F., Jiang, C., Fu, L., 2015. Direct growth of molybdenum disulfide on arbitrary insulating surfaces by chemical vapor deposition. RSC Adv. 5 (6), 4364–4367.

Wang, M., Anghel, A.M., Marsan, B., Cevey Ha, N.-L., Pootrakulchote, N., Zakeeruddin, S.M., Grätzel, M., 2009. CoS supersedes Pt as efficient electrocatalyst for triiodide reduction in dye-sensitized solar cells. J. Am. Chem. Soc. 131 (44), 15976–15977.

Wu, M., Wang, Y., Lin, X., Yu, N., Wang, L., Wang, L., Hagfeldt, A., Ma, T., 2011. Economical and effective sulfide catalysts for dye-sensitized solar cells as counter electrodes. PCCP 13 (43), 19298–19301.

Xin, X., He, M., Han, W., Jung, J., Lin, Z., 2011. Low-cost copper zinc tin sulfide counter electrodes for high-efficiency dye-sensitized solar cells. Angew. Chem. Int. Ed. 50 (49), 11739–11742.

Yang, L., Cui, X., Zhang, J., Wang, K., Shen, M., Zeng, S., Dayeh, S.A., Feng, L., Xiang, B., 2014. Lattice strain effects on the optical properties of MoS2 nanosheets. Sci. Rep. 4, 5649.

Yella, A., Lee, H.-W., Tsao, H.N., Yi, C., Chandiran, A.K., Nazeeruddin, M.K., Diau, E.W.-G., Yeh, C.-Y., Zakeeruddin, S.M., Grätzel, M., 2011. Porphyrin-sensitized solar cells with cobalt (II/III)–based redox electrolyte exceed 12 percent efficiency. Science 334 (6056), 629–634.

Yoon, C.H., Vittal, R., Lee, J., Chae, W.-S., Kim, K.-J., 2008. Enhanced performance of a dye-sensitized solar cell with an electrodeposited-platinum counter electrode.

Electrochim. Acta 53 (6), 2890–2896.
Yu, C., Meng, X., Song, X., Liang, S., Dong, Q., Wang, G., Hao, C., Yang, X., Ma, T., Ajayan, P.M., 2016. Graphene-mediated highly-dispersed MoS2 nanosheets with enhanced triiodide reduction activity for dye-sensitized solar cells. Carbon 100, 474–483.
Yue, G., Lin, J.-Y., Tai, S.-Y., Xiao, Y., Wu, J., 2012. A catalytic composite film of MoS 2/ graphene flake as a counter electrode for Pt-free dye-sensitized solar cells. Electrochim. Acta 85, 162–168.
Yue, G., Wu, J., Lin, J.-Y., Xiao, Y., Tai, S.-Y., Lin, J., Huang, M., Lan, Z., 2013. A counter electrode of multi-wall carbon nanotubes decorated with tungsten sulfide used in dye-sensitized solar cells. Carbon 55, 1–9.
Zeng, H., Liu, G.-B., Dai, J., Yan, Y., Zhu, B., He, R., Xie, L., Xu, S., Chen, X., Yao, W., 2013. Optical signature of symmetry variations and spin-valley coupling in atomically thin tungsten dichalcogenides. Sci. Rep. 3.
Zhang, J., Najmaei, S., Lin, H., Lou, J., 2014. MoS 2 atomic layers with artificial active edge sites as transparent counter electrodes for improved performance of dye-sensitized solar cells. Nanoscale 6 (10), 5279–5283.